### Title
Undoped and Ni-Doped CoO x Surface Modification of Porous BiVO4 Photoelectrodes for Water Oxidation




### Journal
The Journal of Physical Chemistry C, 120(41)

### ISSN
1932-7447



### Authors
Liu, Ya
Guo, Youhong
Schelhas, Laura T
et al.



### Publication Date
2016-10-20

### DOI
10.1021/acs.jpcc.6b08654

Peer reviewed

# Undoped and Ni-doped $CoO_x$ Surface Modification of Porous $BiVO_4$ Photoelectrodes for Water Oxidation

*Ya Liu,[†,‡,¶] Youhong Guo,[§] Laura T. Schelhas,[‖] Mingtao Li,[*,¶] and Joel W. Ager III[*,†,‡]*

[†]Joint Center for Artificial Photosynthesis, [‡]Materials Sciences Division, Lawrence Berkeley National Laboratory, Berkeley, California 94720, United States

[¶]International Research Center for Renewable Energy, State Key Laboratory of Multiphase Flow in Power Engineering, Xi'an Jiaotong University, Shaanxi 710049, China

[§]Department of NanoEngineering, University of California San Diego, 9500 Gilman Dr., La Jolla, California 92093, United States

[‖]Stanford Synchrotron Radiation Lightsource, SLAC National Accelerator Laboratory, Menlo Park, California 94025, United States

ABSTRACT:

Surface modification of photoanodes with oxygen evolution reaction (OER) catalysts is an effective approach to enhance water oxidation kinetics, to reduce external bias, and to improve the energy harvesting efficiency of photoelectrochemical (PEC) water oxidation. Here, the surface of porous $BiVO_4$ photoanodes was modified by the deposition of undoped and Ni-doped $CoO_x$ *via* nitrogen flow assisted electrostatic spray pyrolysis. This newly developed atmospheric pressure deposition technique allows for surface coverage throughout the porous structure with thickness and composition control. PEC testing of modified $BiVO_4$ photoanodes show that after deposition of an undoped $CoO_x$ surface layer, the onset potential shifts negatively by *ca.* 420 mV and the photocurrent density reaches 2.01 $mA \cdot cm^{-2}$ at 1.23 vs. $V_{RHE}$ under AM 1.5G illumination. Modification with Ni-doped $CoO_x$ produces even more effective OER catalysis and yields a photocurrent density of 2.62 $mA \cdot cm^{-2}$ at 1.23 $V_{RHE}$ under AM 1.5G illumination. The valence band X-ray photoelectron spectroscopy and synchrotron-based X-ray absorption spectroscopy results show the Ni doping reduces the Fermi level of the $CoO_x$ layer; the increased surface band bending produced by this effect is partially responsible for the superior PEC performance.

## INTRODUCTION

Artificial photosynthesis is the concept of replicating the natural process of photosynthesis by capturing solar energy in chemical bonds.[1–3] Although the concept dates back to the early 20th century,[4] there has been increasing recent interest in developing artificial photosynthesis schemes which could create a sustainable energy supply and combat the effects of climate change due to fossil fuel combustion.[5–7] In this context, photoelectrochemical (PEC) water splitting is an artificial photosynthesis approach which performs solar to fuel conversion through the generation of hydrogen and oxygen.[8–11]

There are a number of possible device designs and geometries which can perform PEC water splitting.[12] One specific device design uses a tandem photovoltaic approach to generate the requisite potential to drive the water splitting reaction, which is typically ca. 0.6 V above the thermodynamic minimum of 1.23 V.[13–16] Recently, there has been significant research interest in the development of metal oxides as photoanodes for overall water splitting.[17–20] This class of materials tends to have a higher band gap than traditional PV materials such as Si, making them attractive for the top cell in a tandem design.[15]

Bismuth vanadate ($BiVO_4$) has emerged as an attractive photoanode for PEC water splitting and also for fundamental studies of charge separation, transport, and solid-electrolyte interactions.[21] Its bandgap of 2.4 eV gives it a theoretical maximum current density of 7.21 $mA/cm^2$ (see Supporting Information). Recent studies report that $BiVO_4$ has the most negative photocurrent onset potential for water oxidation among all the reported visible light absorbing n-type photoanodes due to its favorable band edge alignment with the water redox potentials.[22] The large onset potential, relative to the $O_2/H_2O$ potential, is advantageous in the design of monolithic

tandems; as a result, monolithic devices with $BiVO_4$ photoanodes have achieved overall solar to $H_2$ conversion efficiencies approaching 5 mol%.[23,24]

In general, surface modification of $BiVO_4$ (and most other photoanodes) with co-catalysts is used to achieve the best performance and stability.[25] Surface modification of photoanodes with OER catalysts is an effective approach to reduce the photocurrent onset potential because it can enhance water oxidation kinetics and reduce external bias.[25–29] For $BiVO_4$, the surface modification should perform OER in the appropriate pH range and also reduce the hole recombination at the $BiVO_4$/catalyst interface. There has been extensive work on the integration of $BiVO_4$ with OER catalysts (see Table S1 for details, Supporting Information). For operation in near-neutral solution (~ pH 7) cobalt-phosphate[30–32] and iron and nickel (oxy)hydroxides[33–35] have been investigated as co-catalysts for $BiVO_4$. For more alkaline conditions (up to pH 13), transition metal oxides, such as cobalt oxides,[36–39] nickel oxides,[37] and $ZnFe_2O_4$,[40] have also been studied.

Choi and co-workers reported that dual-layer FeOOH/NiOOH OER catalysts reduced the charge recombination and increased the PEC performance of $BiVO_4$ photoanodes.[33,34] Dual-layer $CoO_x$/p-type NiO OER catalysts fabricated by Zhong *et al*. have also been reported to enhance PEC water oxidation process for $BiVO_4$ particles deposited on Ti metal substrates.[37] Lichterman *et al*. deposited thin $CoO_x$ layers by atomic layer deposition on spin coated $BiVO_4$ films and demonstrated the enhancement of the PEC performance at high pH.[36] Chang *et al*. used $Co_3O_4$ nanoparticles to modify the surface of $BiVO_4$ film, and obtained a noticeable PEC performance due to the synergetic enhancement of surface reaction kinetics and bulk charge separation.[38]

It is quite evident that an ideal co-catalyst would, by analogy with PV devices,[41] reduce carrier recombination at the semiconductor/catalyst interface while also increase the rate of the desired chemical reaction, OER in this case. Here, we are investigating $CoO_x$ as an OER catalyst; it has

previously been used to modify not only $BiVO_4$ but also other visible light absorbing photoanodes, such as $Fe_2O_3$ and Si.[42,43] The goal of the study was to find a facile method to (1) obtain a continuous coating to cover the surface throughout a porous $BiVO_4$ photoanode, and (2) modify the energetics of the $BiVO_4$/catalyst interface to suppress hole recombination and improve the rate of OER. We found that a nitrogen flow assisted electrostatic spray pyrolysis deposition process could be used to cover the porous $BiVO_4$ structure throughout with the OER catalyst. We also found that doping the surface $CoO_x$ layer with Ni ions by this this new method could produce better PEC performance, in part due to increased band bending induced in the $BiVO_4$.

## EXPERIMENTAL

**Fabrication of porous $BiVO_4$ photoelectrodes.** The detailed fabrication procedures are provided in the Supporting Information. Here we present a brief overview of the procedure, which was adapted from Choi and co-workers.[34,44] First, a film of BiOI nanosheets was deposited on a fluorine-doped tin oxide (FTO) coated glass substrate *via* an electrochemical synthesis route. Some changes were made to the parameters from the literature to optimize the growth: the pH value was adjusted to 1.5, the applied potential was set at -0.2 V vs. Ag/AgCl, and the deposition time was set to 120 seconds.[34,44] Subsequently, excess vanadyl acetylacetonate ($VO(acac)_2$) was used to convert BiOI to $BiVO_4$, while the by-product, vanadium oxide, was removed by etching in alkali solution.

**Surface modification with $CoO_x$ and Ni-doped $CoO_x$.** Nitrogen flow assisted electrostatic spray pyrolysis was used to deposit $CoO_x$ layers on the $BiVO_4$ photoelectrodes. A schematic of the system is shown in Figure 1. A traditional electrospray system consists of a high voltage power supply with connections and injection pumps for the precursors. To this basic set-up, we added a heating plate to perform the pyrolysis, a 3 axis motorized linear positioning stages for horizontal

scanning, and a co-axial nozzle. The homemade co-axial nozzle consists of a long fine needle (250 mm in length, with an outer diameter of 0.41 mm, and an inlet diameter of 0.21 mm) and a short thick needle (55 mm in length, with an outer diameter of 0.84 mm, and an inlet diameter of 1.27 mm). The spray solution was pumped to the inner tube of the co-axial nozzle (pink, in Figure 1), while pressurized nitrogen gas was blown through the outer tube (blue, in Figure 1). The liquid precursor was 2.5 mM cobalt acetylacetonate in ethanol sprayed at a flow rate of 0.5 mL per hour; the flow rate of nitrogen gas was set to 400 mL per minute. After placing the $BiVO_4$ thin film on 350 ºC heating plate for 10 minutes, the distance between the substrate and the tip of the nozzle was adjusted to 2 cm, and the voltage was fixed at 5000 V. A reciprocating scanning pattern was employed, and the deposition time was adjusted by using different steps along the x axis, which can be easily set in the control program.

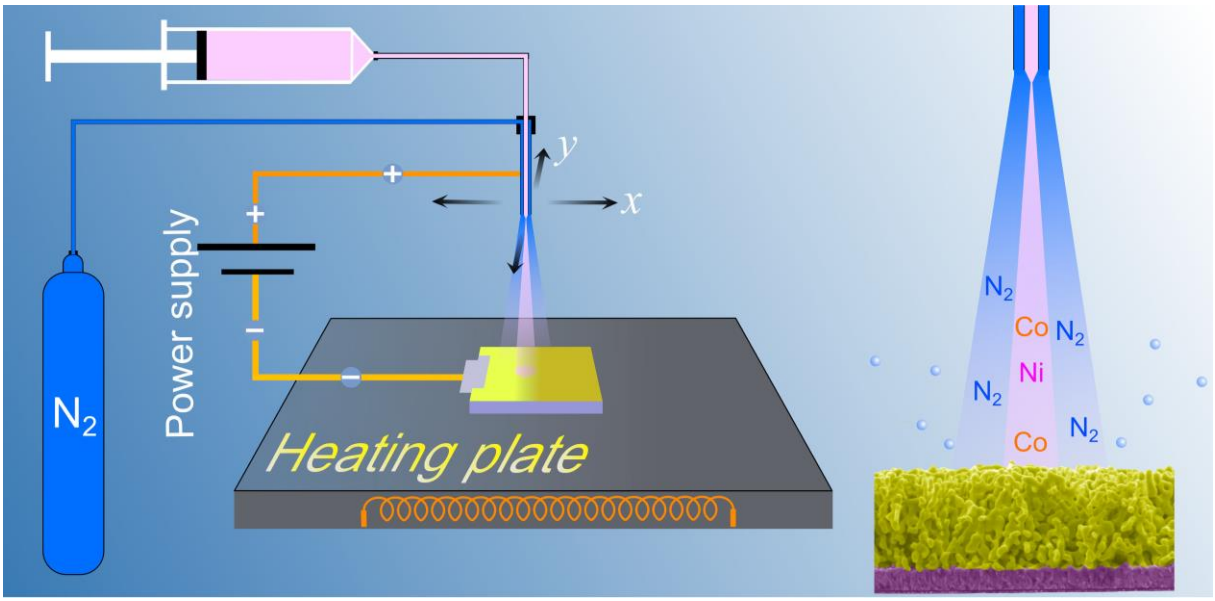


**Figure 1.** Schematic illustration of the nitrogen flow assisted electrostatic spray pyrolysis system. The enlarged schematic on the right depicts the co-axial nozzle.

For a typical deposition, the $BiVO_4$ photoelectrode (50 mm x 25 mm) was placed in the center of the deposition area (60 mm x 35 mm). After completing of the scanning program, the surface modified $BiVO_4$ photoanodes were annealed at 450 ºC for 2 hours in air. For Ni-doped $CoO_x$ surface layer deposition, five different molar percentages of nickel acetate (0.5 mol%, 1 mol%, 2 mol%, 3 mol%, and 4 mol% relative to cobalt acetylacetonate) were added into the spray solution with the rest of procedures being unchanged. For chemical state measurements, a series of thick Ni-doped $CoO_x$ films were prepared by dip-coating heated quartz substrates (100 ºC) into the same precursor solutions followed by the same post anneal treatment, 450 ºC for 2 hours.

**Characterization.** Surface morphology characterization was performed by a JEOL JSM-7800F field emission scanning electron microscope (FE-SEM), and energy dispersive X-ray spectroscopy (EDS) analysis was performed using the installed energy-dispersive X-ray detector, OXFORD INCA. X-ray photoelectron spectroscopy (XPS) measurements were conducted using a Kratos spectrometer (Axis UltraDLD) with monochromatic Al Kα radiation ($h\nu$ = 1486.69 eV). The C 1s signal centered at 284.8 eV, adventitious carbon, was used to calibrate the binding energies. The reflectance and transmittance spectra of the films were obtained from a double-beam UV4100 UV-vis-NIR spectrophotometer equipment with an integrating sphere detector. X-ray absorption spectroscopy (XAS), near-edge structure (XANES) and extended X-ray absorption fine-structure (EXAFS) were also used to probe the atomic structure of the surface layer. The XAS, XANES, and EXAFS measurements were performed on beamline 7-3 at the Stanford Synchrotron Radiation Lightsource (SSRL). The synchrotron wide-angle X-ray scattering (WAXS) diffraction measurement was performed on beam line 11-3 at the Stanford Synchrotron Radiation Lightsource (SSRL). The incidence angle was 2 degrees, and the x-ray energy was 12.735 KeV. The conventional wide-angle X-ray scattering (WAXS) diffraction analysis was performed with an

X'pert PRO diffractometer (X' Pert PRO MPD, PANalytical, the Netherlands, Cu Ka irradiation, $\lambda = 1.541874$ Å).

**Photoelectrochemical measurements.** The current density vs. voltage (J-V) characteristics were evaluated in a three-electrode system which includes a self-made electrode holder using a CHI 760D scanning potentiostat (CH Instruments). The prepared photoelectrode was used as working electrode. Silver/silver chloride (Ag/AgCl), and a platinum foil served as reference and counter electrodes, respectively. The electrolyte was aqueous 0.5 M $Na_2SO_4$. The solar simulator was a 500 W xenon lamp coupled to an AM1.5 filter in order to yield a light intensity of 100 $mW \cdot cm^{-2}$, as calibrated by a silicon solar cell from Newport Corporation. The measured potential *vs.* the Ag/AgCl reference electrode was converted to the reversible hydrogen electrode (RHE) scale using the formula $V_{RHE} = V_{Ag/AgCl} + 0.059\ pH + 0.1976\ V$.[45] The incident photon-to-charge conversion efficiency (IPCE) was measured with an home-built setup using a three electrode system. A 150 W Xe lamp (Newport) was used as the light source. The flux of photons impinging on the sample was calibrated by a Thorlabs FDS1010-CAL calibrated Si photodiode. A Gamry Reference 600 potentiostat was used to control the applied potential and current.

## RESULTS AND DISCUSSION

**Structure of $BiVO_4/CoO_x$ photoanodes.** The porous structure of the $BiVO_4$ film is depicted in Fig. 2; additional SEM images are shown in Fig. S1, indicating the pore size ranges from tens of nanometers to hundreds of nanometers. This porous structure was the basis for all the subsequent surface modified photoanodes. Figure 2 also displays the evolution of the microstructure of the $BiVO_4$ modified by $CoO_x$ as the deposition time was increased from 30 minutes to 4 hours. As the deposition time increases, the surface layer becomes a bit thicker, but the porous structure remains. After 4 hours of $CoO_x$ deposition, some additional interconnections in the structure are observed,

as indicated by white arrows in Fig. 2. Synchrotron x-ray diffraction was used assess the presence of crystalline phases in a $BiVO_4/CoO_x$ photoanode (4 hours of deposition). As shown in Fig. S2, all observed peaks could be assigned to either monoclinic $BiVO_4$ or the FTO substrate, indicating that the $CoO_x$ surface layer is probably amorphous or has only very small crystallites.

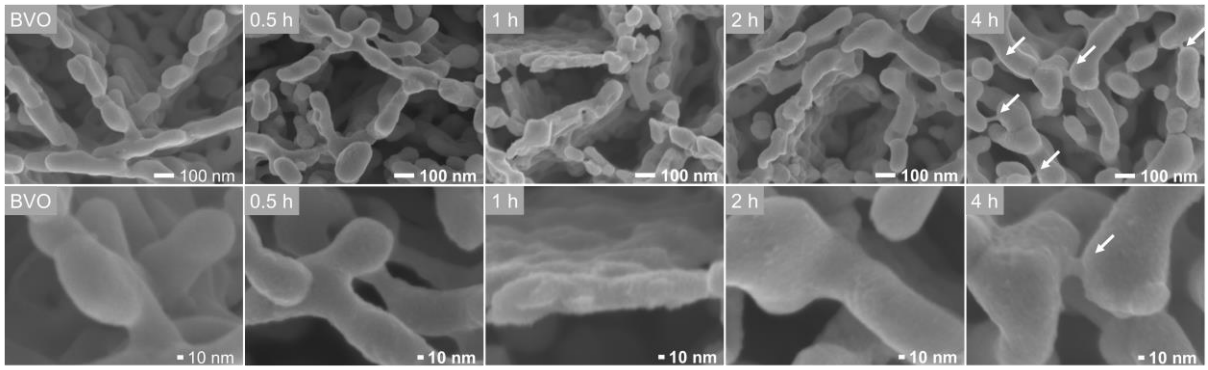


**Figure 2.** FESEM images of pristine $BiVO_4$ (BVO) and $BiVO_4/CoO_x$ photoanodes with spray pyrolysis deposition times of a half hour (0.5 h), 1 hour (1 h), 2 hours (2 h), and 4 hours (4 h). After 4 hours of deposition and annealing step, interconnections within the porous structure are observed, as indicated by the white arrows in (4 h).

For optimal integration of the OER catalyst with the $BiVO_4$, a continuous coating of $CoO_x$ throughout the porous structure is desired. In nitrogen flow assisted electrostatic spray pyrolysis, the gas flow is used to break up the droplets which form on the surface of $BiVO_4$ and drive the precursor into the porous structure. We assessed the vertical uniformity of the $CoO_x$ incorporation by performing EDS line scans on cross sections of the photoanode. Figure 3(a) shows that the incorporation of $CoO_x$ into the porous structure after 4 hours of deposition and annealing step is quite uniform. In contrast, for a control sample fabricated without the $N_2$ gas flow, Co is concentrated at the top of the film, as shown in Fig 3(b).

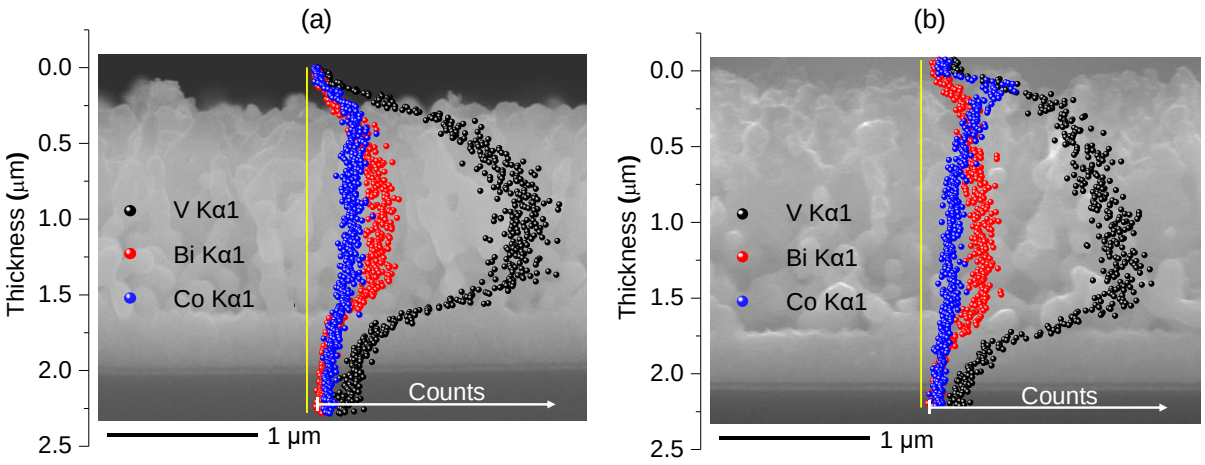


**Figure 3.** EDS line-scan profile of Co, Bi, V for (a) as prepared $BiVO_4/CoO_x$ photoanode by nitrogen flow assisted electrostatic spray pyrolysis and (b) the photoanode prepared without $N_2$ gas flow. The surface layer deposition time was 4 hours.

Atomic layer deposition (ALD) has been used to form conformal coatings in high surface area structures, including water oxidation photoelectrodes.[43,46–49] However, this process requires a low pressure environment and suitable precursor molecules for growth of the desired materials.[50] In contrast, the nitrogen flow assisted electrostatic spray pyrolysis process developed here operates at atmospheric pressure with a simpler precursor chemistry. Also, as shown later, the composition of deposited layers can be controlled by adjusting the components in the precursor solutions. Furthermore, this method could be used for the large area deposition by employing an array of nozzles to reduce the deposition time, making it much more industrially relevant compared to ALD. Also, in contrast to ALD, the size of samples which can be treated is not limited by the practical size of the vacuum chamber.

The chemical states of the elements Co, Bi and V in the films were investigated by high-resolution XPS. Co 2p, Bi 4f, and V 2p spectra are shown in Figure 4. With increasing $CoO_x$ deposition time, the peaks of Co 2p start to appear while the peaks of Bi 4f and V 2p become less

intense. After 4 hours of deposition, the Bi 4f and V 2p peaks are still visible. As XPS is sensitive to near-surface elements only,[51] we estimate that the $CoO_x$ layers are less than 10 nm thick.

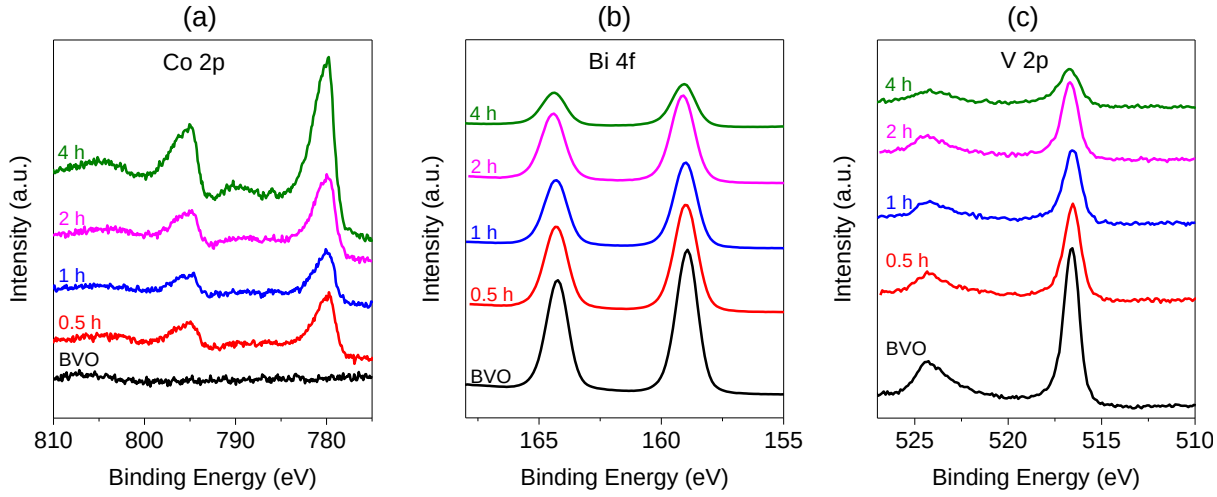


**Figure 4.** High-resolution XPS spectra of Co 2p (a), Bi 4f (b), and V 2p (c) for pristine $BiVO_4$ (BVO) and $BiVO_4/CoO_x$ photoanodes with different deposition times of a half hour (0.5 h), 1 hour (1 h), 2 hours (2 h), and 4 hours (4 h).

**PEC evaluation of $BiVO_4/CoO_x$ photoanodes.** The PEC performances of the samples were evaluated using illumination from the back side (through the FTO substrate). This geometry was chosen because, for $BiVO_4$ photoanodes, back side illumination has been shown to be more tolerant to charge recombination than the front side illumination (from electrolyte to photoanode).[52,53] In Figure 5, the photocurrent-potential (J-V) curves show that all the surface modified samples display significant cathodic onset potential shifts compared with the unmodified control. The pristine $BiVO_4$ photoanode exhibits the onset of water oxidation at 0.77 vs. $V_{RHE}$ in 0.5 M $Na_2SO_4$ electrolyte. The onset potential of all of the $CoO_x$ modified photoanodes is cathodically shifted by over 400 mV, to 0.35 vs. $V_{RHE.}$ While all the modified photoanodes show similar onset potentials, the current density is dependent on the deposition time. The current density after a 0.5 h of deposition is only slightly improved at 1.23 vs. $V_{RHE}$ AM 1.5G illumination;

we suspect that the $BiVO_4$ surface is not completely covered. The sample with 1 hour of deposition shows the highest photocurrent density, 2.01 $mA \cdot cm^{-2}$ at 1.23 $V_{RHE}$.

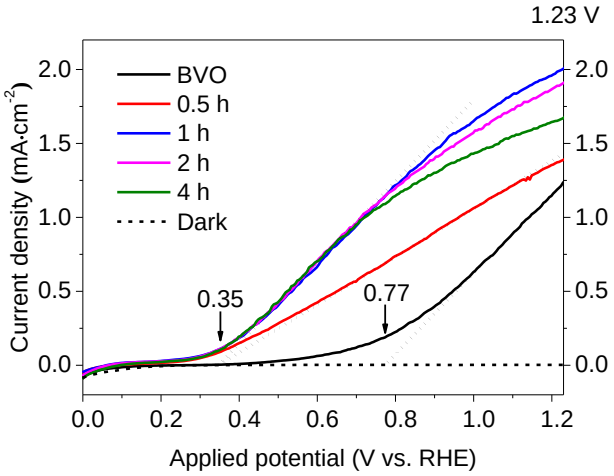


**Figure 5.** J-V curves of pristine $BiVO_4$ (BVO) and $BiVO_4/CoO_x$ photoanodes with different deposition times of a half hour (0.5 h), 1 hour (1 h), 2 hours (2 h), and 4 hours (4 h). J-V measurement was performed in a 0.5 M $Na_2SO_4$ aqueous solution under AM 1.5 G illumination. The onset potential is determined by the intersection point of the zero current density and the tangent (the dotted line) at maximum slope of photocurrent.

**Doping of Ni ions inside $CoO_x$ layer.** $CoO_x$ surface modification provides a significant enhancement in the current density, but it is still far from the maximum value (4.76 $mA/cm^2$) which could be obtained from the porous $BiVO_4$ photoanodes based on their absorption spectra (see the details in the Supporting Information). The nitrogen flow assisted electrostatic spray pyrolysis process makes it very easy to produce metal-doped surface layers by simply adding the dopant metal ions into the precursor solution. Therefore, we doped small amount of Ni (0.5 mol%, 1 mol%, 2 mol%, 3 mol%, and 4 mol%) inside the $CoO_x$ layer by simply adding Ni ions in the precursor solution, and keeping the deposition time at 1 hour, which was the deposition time producing the optimal performance for undoped $CoO_x$. The surface morphology of the doped surface layers

(Figure S3) is similar to that of the un-doped $CoO_x$ surface layers (Figure 2, 1 h). To verify that the dopant Ni atoms were incorporated within the $CoO_x$, high-resolution XPS was employed. However, it was difficult to directly detect the tiny amount of Ni from the $BiVO_4$/Ni-$CoO_x$ photoanode, because of the interference from signals from the other metal ions, Co, Bi and V. Therefore, we prepared a series of thicker Ni-doped $CoO_x$ films on quartz using the same electrostatic spray precursor solution to remove the interference of Bi and V. The high-resolution XPS spectra of Ni 2p are shown in Figure 6a; Co 2p spectra for Ni-doped $CoO_x$ films are shown in Figure 6b. Although all peaks of Ni 2p for Ni-doped samples are relatively weak, they show clearly an increase in intensity as the atomic ratio of Ni in precursor solution increases while the Co 2p remain unchanged. These XPS results verify that Ni is incorporated inside the surface modification layers.

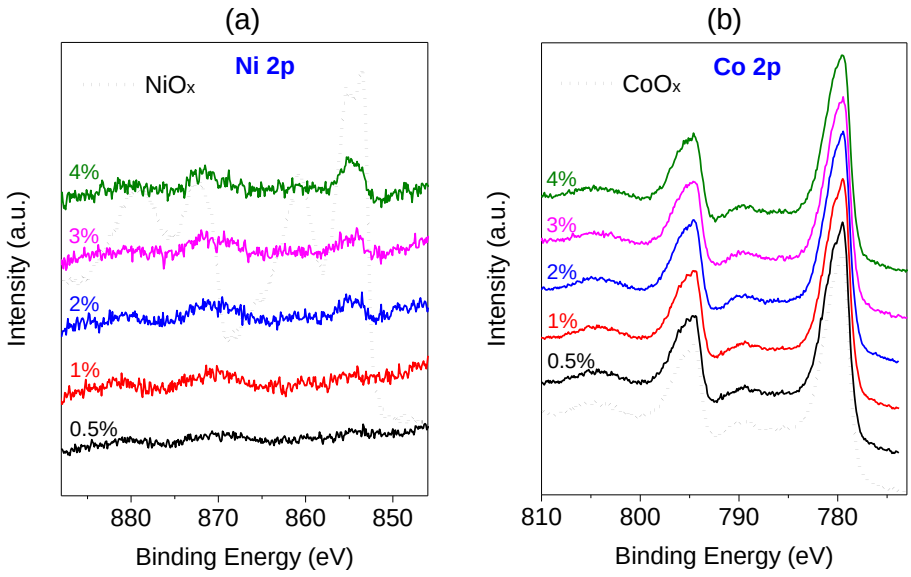


**Figure 6.** High-resolution XPS spectra of Ni 2p (a) and Co 2p (b) for Ni-doped $CoO_x$ films with atomic ratios of Ni: 0.5 mol%, 1 mol%, 2 mol%, 3 mol%, and 4 mol%. The dashed line in A represents the spectrum of from pure nickel oxide. The films were prepared by dip coating the

same electrostatic spray precursor solutions on quartz substrates and employing the same post anneal treatment.

The PEC performance of the samples after Ni doping was evaluated by J-V measurements. The results are shown in Figure S4, indicating 1 mol% Ni doping produces the highest photocurrent density. Figure 7a shows a comparison of the J-V curves for the pristine $BiVO_4$, pure $CoO_x$ surface modified $BiVO_4$, and 1 mol% Ni-doped $CoO_x$ surface modified $BiVO_4$ photoelectrodes. For 1 mol% Ni doping, the photocurrent density reaches to 2.62 $mA \cdot cm^{-2}$ at 1.23 $V_{RHE}$ under AM 1.5G illumination, which is *ca.* 30 mol% greater than the photocurrent density of the pure $CoO_x$ surface modified $BiVO_4$ photoanode. Also, Figure 7a shows that Ni-doping does not shift the onset potential. In Figure 7b, the IPCE spectra indicate that the surface layer does not change the spectral response ranges, and the enhanced IPCE for the surface modified photoanodes is consistent with the J-V results.

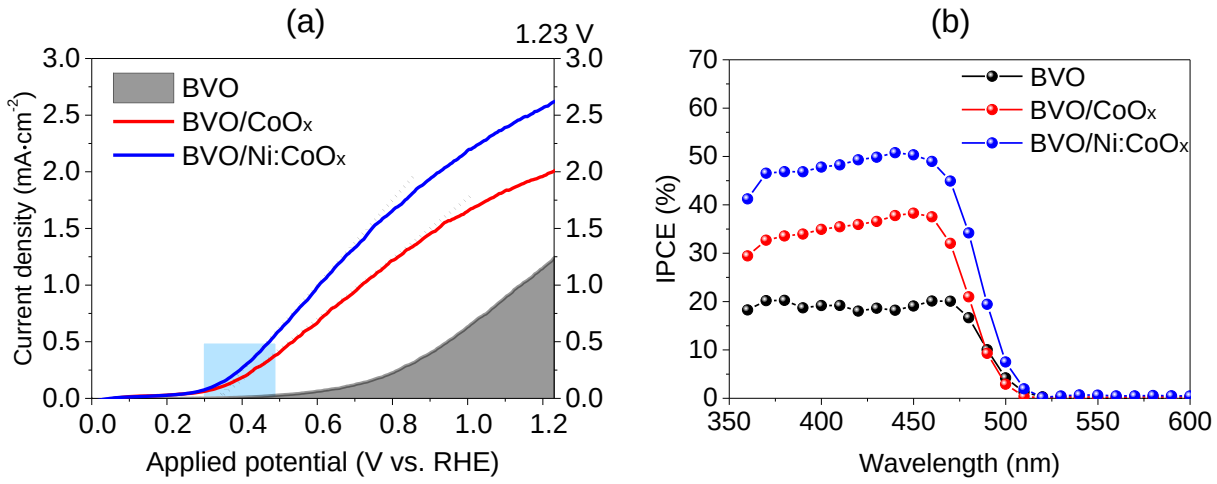


**Figure 7.** (a) J-V curves and (b) IPCE spectra of pristine $BiVO_4$ (black), $CoO_x$ surface modified $BiVO_4$(red), and 1 mol% Ni-doped $CoO_x$ surface modified $BiVO_4$ photoelectrodes (blue). The dotted line in (a) is the tangent at maximum slope of photocurrent. The surface layer deposition time is 1 hour. J-V measurement was performed in a 0.5 M $Na_2SO_4$ aqueous solution under AM

1.5 G illumination. During the IPCE measurement, the applied potential of the working electrodes was maintained at 1.23 $V_{RHE}$.

**$BiVO_4$/Ni-doped $CoO_x$ PEC mechanism.** To investigate why Ni-doped $CoO_x$ produces a better PEC performance, we will delineate the efficiency of (1) charge generation, (2) charge separation and (3) charge injection/catalysis in a systematic way. First, the absorption spectra were measured to evaluate charge generation, as shown in Figure 8a. The band gap energy ($E_g$) of the bare-$BiVO_4$ was evaluated by a Tauc plot (Figure 8b) to be approximately 2.42 eV corresponding to a wavelength of 512 nm. Although the photoanode absorbs more light after the surface modification, it is mostly above the photosensitivity edge (denoted by the IPCE spectra in Figure 7b). Also, Ni doping produces almost no effect on light absorption (Fig. 8a). Thus, the photocurrent enhancement of surface modified $BiVO_4$ is not attributed to greater light absorption.

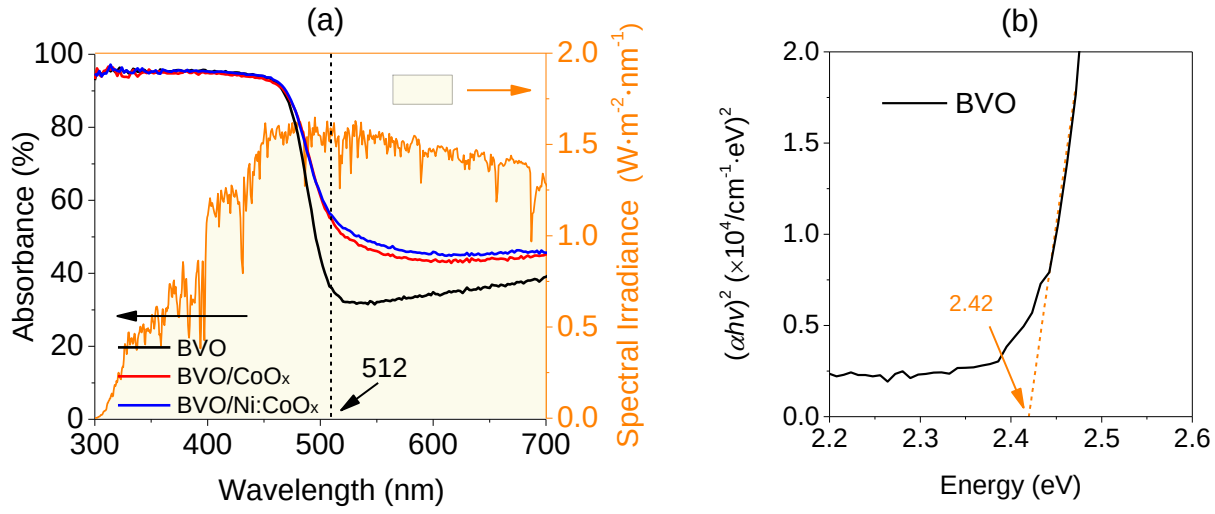


**Figure 8.** Absorptance spectra (a) and the Tauc plots (b) of pristine $BiVO_4$ (black), $CoO_x$ surface modified $BiVO_4$(red), and 1 mol% Ni-doped $CoO_x$ surface modified $BiVO_4$ photoelectrodes (blue). The surface layer deposition time was 1 hour. The background spectrum (orange) is the AM1.5

Global spectrum with an integrated power of 100 mW/cm$^2$ (from National Renewable Energy Laboratory).

To quantify the catalytic activity contributions of different cobalt-containing surface layers, the charge separation efficiency ($\eta_{cs}$) and the charge injection efficiency ($\eta_{ci}$) were evaluated (details in the Supporting Information). The photocurrent for water splitting, $J_{\text{photocurrent}}$, is the product of the rate of photon absorption ($J_{\text{absorbed}}$), $\eta_{\text{cs}}$, and $\eta_{\text{ci}}$, as shown in Eq. 1 of the Supporting Information. $\eta_{cs}$ is the yield of the charge separation in the bulk, and $\eta_{ci}$ is the yield of the holes which reach the surface and perform oxidative chemistry in the electrolyte. As shown in Figure 9, $\eta_{cs}$ reveals no significant increase with surface modification, while the cobalt-containing surface layer generates an improvement in $\eta_{ci}$, indicating the cobalt-containing surface layer functions as an OER catalyst. Also, the Ni-doped $CoO_x$ layer produces a higher $\eta_{ci}$ than pure $CoO_x$ layer does, suggesting better OER kinetics for the doped layer. However, the evaluation of the OER performance of the surface layers (without $BiVO_4$) in the dark shows that the OER activity of Ni-doped $CoO_x$ and undoped $CoO_x$ are similar (Figure S6).

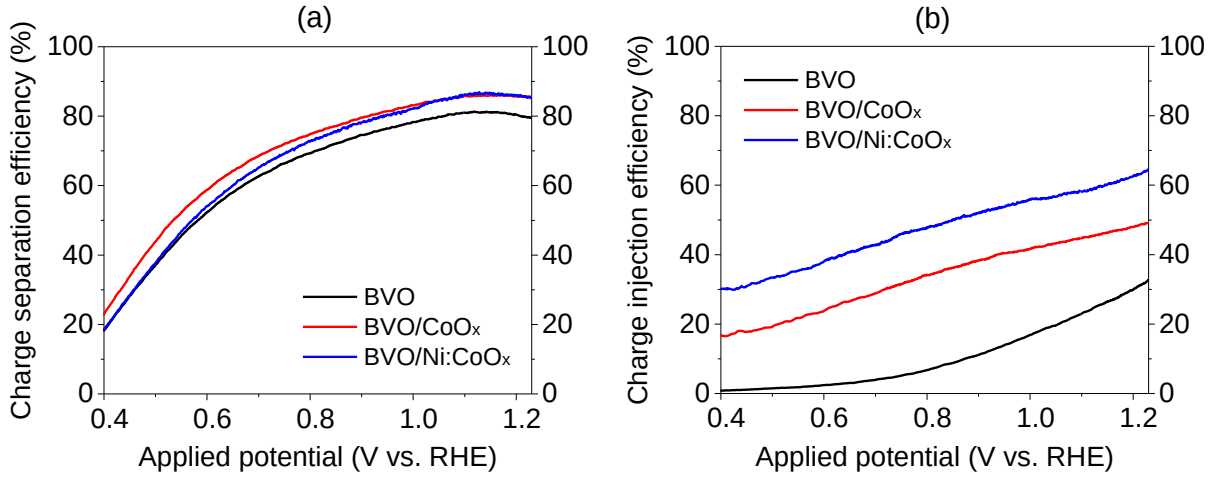

**Figure 9.** Charge separation efficiency (a) and charge injection efficiency (b) of pristine $BiVO_4$ (black), $CoO_x$ surface modified $BiVO_4$ (red), and 1 mol% Ni-doped $CoO_x$ surface modified $BiVO_4$ photoelectrodes (blue). The surface layer deposition time is 1 hour.

Thus, to investigate whether there is a specific interface effect caused by doping the surface layer, the band structure was studied by valence band XPS spectra, as shown in Figure 10. The photoemission onset, the energetic difference between the Fermi energy and the valence band edge, of the pristine $BiVO_4$ is *ca.* 1.8 eV (black curve in Figure 10), indicating a n-type character.[54] The photoemission onset of the $CoO_x$ surface layer is *ca.* 0.71 eV (red curve in Figure 10), which is in agreement with the $Co_3O_4$ published literature.[55] For the Ni-doped $CoO_x$ surface layer, the photoemission onset is close to the Fermi level (blue curve in Figure 10), showing that the Ni-doped $CoO_x$ can be identified as a p-type material.

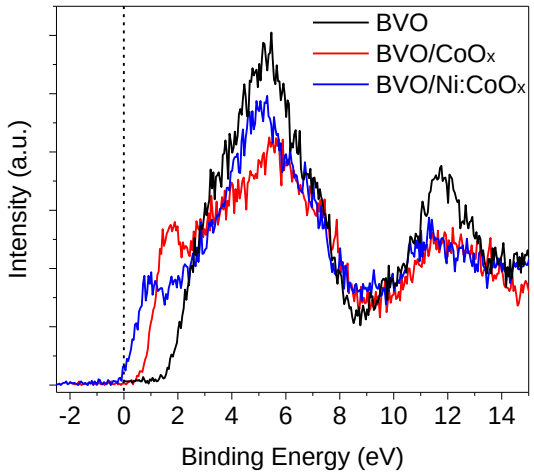


**Figure 10.** Valence band XPS spectra of pristine $BiVO_4$ (black), $CoO_x$ surface modified $BiVO_4$(red), and 1 mol% Ni-doped $CoO_x$ surface modified $BiVO_4$ photoelectrodes (blue). The surface layer deposition time is 1 hour. Fermi level lies at 0 binding energy (black dotted line).

To gain further insight into the atomic structure, XAS were collected at the Co K-edge on the samples with a relatively thick surface layer (4 hours of deposition), as shown in Figure 11. The

XANES gives more information on the symmetry and the electronic structure, while the EXAFS is more sensitive to bond distances, local disorder, and coordination numbers.[56] EXAFS spectrum is usually interpreted in real (k) or in Fourier transform (R) space.[56] Although the XANES spectra (Figure 11a) of samples without and with Ni doping are very similar, the $k^3$-weighted *k*-space EXAFS spectra (Figure 11b) show the shape of the curve has a discernable change for wave vectors greater than 10 $Å^{-1}$, indicating there should be a change in the *R*-space. From the EXAFS spectra in R-space, four clear peaks are observed. They are all consistent with the published peaks for $Co_3O_4$, indicating the $CoO_x$ prepared in this work mostly likely has the short range order of $Co_3O_4$.[57–60] There are two types of cobalt ions with different oxidation states in spinel $Co_3O_4$: two $Co^{3+}$ ions in the octahedral site and one $Co^{2+}$ ion in the tetrahedral site.[61] Reported fitting results show the first peak (I in Figure 11c) is consistent with the convolution of two Co–O distances coming from the tetrahedral and octahedral Co coordination respectively.[58,59] The second peak (II in Figure 11c) corresponds to the $Co^{3+}$–$Co^{3+}$ distance.[58,60] The third peak (III in Figure 11c) is assigned to $Co^{3+}$–$Co^{2+}$ and $Co^{3+}$–$Co^{2+}$distances.[58,60] The fourth peak (IV in Figure 11c) is attributed to higher Co−Co and Co−O shells. We do find that the second peak (II in Figure 11c) exhibits a slight but observable shift in *R*-space; it is possible this shift is due to Ni incorporation into the $CoO_x$. Pattengale *et al.* also found a similar peak shift in the EXAFS spectrum of Bi $L_3$-edge in W-doped $BiVO_4$.[62] Considering both the EXAFS results and the clear shift of the valence band edge (Fig. 10), it is suggested that Ni incorporates into the $CoO_x$ lattice as opposed to forming a composite structure.

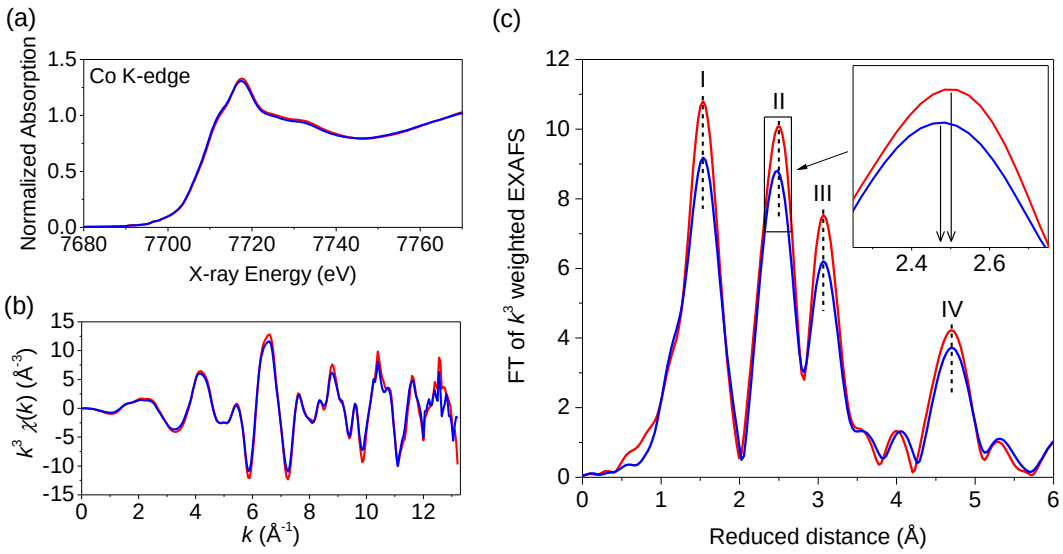


**Figure 11.** (a) XANES spectra, (b) $k^3$-weighted $k$-space EXAFS spectra, and (c) Fourier-transformed (FT) EXAFS spectra in $R$-space of the samples collected at the Co K-edge. Red trace: $CoO_x$ surface modified $BiVO_4$. Blue trace: 1 mol% Ni-doped $CoO_x$ surface modified $BiVO_4$. The deposition time of the surface layer was controlled at 4 hours.

Considering the work functions of monoclinic $BiVO_4$ (5.27 eV)[54] and $Co_3O_4$ (6.1 eV)[63], the interface band diagram for the n-type $BiVO_4/CoO_x$ heterojunction is shown schematically in Figure 12(c). Without Ni doping, band bending occurs at the surface because the work function of the surface layer is larger than that of the bulk $BiVO_4$. This band bending assists the extraction of photo-induced holes out of the photoanode. With Ni doping, the Fermi level of the surface layer becomes lower, increasing the band bending at the surface. This enhanced band bending can accelerate the transfer of the electrons from the surface area, and thus promote the OER.[64] However, under the conditions used to evaluate $\eta_{cs}$ and $\eta_{ci}$ (presence of a hole scavenger $SO_3^{2-}$), the photo generated surface holes are consumed very rapidly. In this case, the enhanced charge transfer enabled by the larger band bending has only a small effect, as can be seen in Figures 9a and S5.

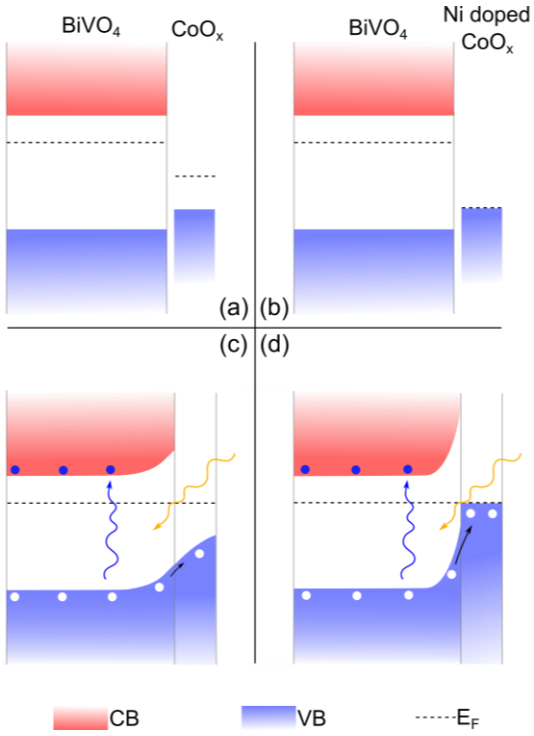


**Figure 12.** Schematic band diagram of the hole transport through the bulk n type $BiVO_4$ and p type cobalt-containing surface layer. (a) $CoO_x/BiVO_4$ before contact; (b) Ni-doped $CoO_x/BiVO_4$ before contact; (c) $CoO_x/BiVO_4$ after contact; (d) Ni-doped $CoO_x/BiVO_4$ after contact.

## CONCLUSIONS

Thin $CoO_x$ and Ni-doped $CoO_x$ layers were uniformly deposited on the surface of a porous $BiVO_4$ photoanode via a new method, nitrogen flow assisted electrostatic spray pyrolysis. This new surface coating method for high surface area structures can be operated under atmospheric conditions with facile control of layer thickness and composition and thus has broad prospects for industrial as well as scientific applications. Porous $BiVO_4$ photoanodes with surfaces modified with this method have improved performance for PEC water oxidation. With the undoped $CoO_x$ layer modification, the photocurrent density reaches 2.01 $mA \cdot cm^{-2}$ at 1.23 $V_{RHE}$ under AM 1.5G illumination, and the onset potential cathodically shifts, *ca.* 420 mV. Ni-doping of the surface layer

leads to further improvements in performance. At 1 mol% Ni doping, the photocurrent density can reach 2.62 $mA \cdot cm^{-2}$ at 1.23 $V_{RHE}$ under AM 1.5G illumination. Valence band XPS and synchrotron EXAFS were used to show that Ni doping enhances the band bending near the surface by lowering the Fermi level of the cobalt-containing surface layer, thus producing the improved OER.

## ASSOCIATED CONTENT

**Supporting Information.** Detailed fabrication procedures; supplemental structural characterization data; supplemental photoelectrochemical measurement data; efficiency evaluation methods; OER performance of the surface layer; Mott-Schottky measurement; stability test results; literature review of OER catalyst modification of $BiVO_4$.

## AUTHOR INFORMATION


### Corresponding Authors

*Email: mingtao@mail.xjtu.edu.cn, Tel: (+86) 29-8266-8296; *Email: JWAger@lbl.gov, Tel: +1 510 486 6715


### Author Contributions

The manuscript was written through contributions of all authors. All authors have given approval to the final version of the manuscript.

## ACKNOWLEDGMENT


We thank Erik Nelson and Matthew Latimer for XAS and EXAFS analysis, Mark Hettick for assistance with IPCE measurements, Penghui Guo and Xiao Zhang for assistance with XPS measurements, and Sudhanshu Shukla for helpful discussions on the XAS analysis. Synthesis, structural (SEM, XRD, XPS) and optical characterization, and the J-V measurements were

supported by the National Natural Science Foundation of China (No. 51302211). IPCE, Chronoamperometry, EIS, WAXS, and XAS measurements were supported by the Joint Center for Artificial Photosynthesis, a DOE Energy Innovation Hub, supported through the Office of Science of the U.S. Department of Energy under Award No. DE-SC0004993. Use of the Stanford Synchrotron Radiation Lightsource, SLAC National Accelerator Laboratory, is supported by the U.S. Department of Energy, Office of Science, Office of Basic Energy Sciences under Contract No. DE-AC02-76SF00515. Y.L. acknowledges fellowship support from the China Scholarship Council (CSC).

## REFERENCES

(1) Sugiyama, M.; Fujii, K.; Nakamura, S. *Solar to Chemical Energy Conversion: Theory and Application*; Lecture Notes in Energy; Springer, 2016.

(2) Rozhkova, E. A.; Ariga, K. *From Molecules to Materials: Pathways to Artificial Photosynthesis*; Springer, 2015.

(3) Kim, D.; Sakimoto, K. K.; Hong, D.; Yang, P. Artificial Photosynthesis for Sustainable Fuel and Chemical Production. *Angew. Chemie Int. Ed.* **2015**, *54*, 3259–3266.

(4) Ciamician, G. The Photochemistry of the Future. *Science* **1912**, *36*, 385–394.

(5) Tachibana, Y.; Vayssieres, L.; Durrant, J. R. Artificial Photosynthesis for Solar Water-Splitting. *Nat. Photonics* **2012**, *6*, 511–518.

(6) Faunce, T. A.; Lubitz, W.; Rutherford, A. W. (Bill); MacFarlane, D.; Moore, G. F.; Yang, P.; Nocera, D. G.; Moore, T. A.; Gregory, D. H.; Fukuzumi, S.; et al. Energy and

Environment Policy Case for a Global Project on Artificial Photosynthesis. *Energy Environ. Sci.* **2013**, *6*, 695.

(7) Herron, J. A.; Kim, J.; Upadhye, A. A.; Huber, G. W.; Maravelias, C. T. A General Framework for the Assessment of Solar Fuel Technologies. *Energy Environ. Sci.* **2015**, *8*, 126–157.

(8) Walter, M. G.; Warren, E. L.; McKone, J. R.; Boettcher, S. W.; Mi, Q.; Santori, E. A.; Lewis, N. S. Solar Water Splitting Cells. *Chem. Rev.* **2010**, *110*, 6446–6473.

(9) Liao, L.; Zhang, Q.; Su, Z.; Zhao, Z.; Wang, Y.; Li, Y.; Lu, X.; Wei, D.; Feng, G.; Yu, Q.; et al. Efficient Solar Water-Splitting Using a Nanocrystalline CoO Photocatalyst. *Nat. Nanotechnol.* **2014**, *9*, 69–73.

(10) Ager, J. W.; Shaner, M. R.; Walczak, K. A.; Sharp, I. D.; Ardo, S. Experimental Demonstrations of Spontaneous, Solar-Driven Photoelectrochemical Water Splitting. *Energy Environ. Sci.* **2015**, *8*, 2811–2824.

(11) Miller, E. L. Photoelectrochemical Water Splitting. *Energy Environ. Sci.* **2015**, *8*, 2809–2810.

(12) Nielander, A. C.; Shaner, M. R.; Papadantonakis, K. M.; Francis, S. A.; Lewis, N. S. A Taxonomy for Solar Fuels Generators. *Energy Environ. Sci.* **2015**, *8*, 16–25.

(13) Weber, M.; Dignam, M. Splitting Water with Semiconducting photoelectrodes—Efficiency Considerations. *Int. J. Hydrogen Energy* **1986**, *11*, 225–232.

(14) Hu, S.; Xiang, C.; Haussener, S.; Berger, A. D.; Lewis, N. S. An Analysis of the Optimal Band Gaps of Light Absorbers in Integrated Tandem Photoelectrochemical Water-Splitting Systems. *Energy Environ. Sci.* **2013**, *6*, 2984.

(15) Prévot, M. S.; Sivula, K. Photoelectrochemical Tandem Cells for Solar Water Splitting. *J. Phys. Chem. C* **2013**, *117*, 17879–17893.

(16) Döscher, H.; Geisz, J. F.; Deutsch, T. G.; Turner, J. A. Sunlight Absorption in Water – Efficiency and Design Implications for Photoelectrochemical Devices. *Energy Environ. Sci.* **2014**, *7*, 2951–2956.

(17) Sivula, K. Metal Oxide Photoelectrodes for Solar Fuel Production, Surface Traps, and Catalysis. *J. Phys. Chem. Lett.* **2013**, *4*, 1624–1633.

(18) Sivula, K.; van de Krol, R. Semiconducting Materials for Photoelectrochemical Energy Conversion. *Nat. Rev. Mater.* **2016**, *1*, 15010.

(19) Liu, Y.; Li, J.; Li, W.; He, H.; Yang, Y.; Li, Y.; Chen, Q. Electrochemical Doping Induced In Situ Homo-Species for Enhanced Photoelectrochemical Performance on $WO_3$ Nanoparticles Film Photoelectrodes. *Electrochim. Acta* **2016**, *210*, 251–260.

(20) Liu, Y.; Li, J.; Tang, H.; Li, W.; Yang, Y.; Li, Y.; Chen, Q. Enhanced Photoelectrochemical Performance of Plate-like $WO_3$ Induced by Surface Oxygen Vacancies. *Electrochem. commun.* **2016**, *68*, 81–85.

(21) Park, Y.; McDonald, K. J.; Choi, K.-S. Progress in Bismuth Vanadate Photoanodes for Use in Solar Water Oxidation. *Chem. Soc. Rev.* **2013**, *42*, 2321–2337.

(22) Kim, T. W.; Ping, Y.; Galli, G. A.; Choi, K.-S. Simultaneous Enhancements in Photon Absorption and Charge Transport of Bismuth Vanadate Photoanodes for Solar Water Splitting. *Nat. Commun.* **2015**, *6*, 8769.

(23) Abdi, F. F.; Han, L.; Smets, A. H. M.; Zeman, M.; Dam, B.; van de Krol, R. Efficient Solar Water Splitting by Enhanced Charge Separation in a Bismuth Vanadate-Silicon Tandem Photoelectrode. *Nat. Commun.* **2013**, *4*, 2195.

(24) Han, L.; Abdi, F. F.; van de Krol, R.; Liu, R.; Huang, Z.; Lewerenz, H.-J.; Dam, B.; Zeman, M.; Smets, A. H. M. Efficient Water-Splitting Device Based on a Bismuth Vanadate Photoanode and Thin-Film Silicon Solar Cells. *ChemSusChem* **2014**, *7*, 2832–2838.

(25) Hu, S.; Lewis, N. S.; Ager, J. W.; Yang, J.; McKone, J. R.; Strandwitz, N. C. Thin-Film Materials for the Protection of Semiconducting Photoelectrodes in Solar-Fuel Generators. *J. Phys. Chem. C* **2015**, *119*, 24201–24228.

(26) Suntivich, J.; May, K. J.; Gasteiger, H. A.; Goodenough, J. B.; Shao-Horn, Y. A Perovskite Oxide Optimized for Oxygen Evolution Catalysis from Molecular Orbital Principles. *Science* **2011**, *334*, 1383–1385.

(27) McCrory, C. C. L.; Jung, S.; Peters, J. C.; Jaramillo, T. F. Benchmarking Heterogeneous Electrocatalysts for the Oxygen Evolution Reaction. *J. Am. Chem. Soc.* **2013**, *135*, 16977–16987.

(28) Yagi, S.; Yamada, I.; Tsukasaki, H.; Seno, A.; Murakami, M.; Fujii, H.; Chen, H.; Umezawa, N.; Abe, H.; Nishiyama, N.; et al. Covalency-Reinforced Oxygen Evolution Reaction Catalyst. *Nat. Commun.* **2015**, *6*, 8249.

(29) McCrory, C. C. L.; Jung, S.; Ferrer, I. M.; Chatman, S. M.; Peters, J. C.; Jaramillo, T. F. Benchmarking Hydrogen Evolving Reaction and Oxygen Evolving Reaction Electrocatalysts for Solar Water Splitting Devices. *J. Am. Chem. Soc.* **2015**, *137*, 4347–4357.

(30) Kanan, M. W.; Nocera, D. G. In Situ Formation of an Oxygen-Evolving Catalyst in Neutral Water Containing Phosphate and $Co^{2+}$. *Science* **2008**, *321*, 1072–1075.

(31) Pilli, S. K.; Furtak, T. E.; Brown, L. D.; Deutsch, T. G.; Turner, J. A.; Herring, A. M. Cobalt-Phosphate (Co-Pi) Catalyst Modified Mo-Doped $BiVO_4$ Photoelectrodes for Solar Water Oxidation. *Energy Environ. Sci.* **2011**, *4*, 5028.

(32) Zhong, D. K.; Choi, S.; Gamelin, D. R. Near-Complete Suppression of Surface Recombination in Solar Photoelectrolysis by "Co-Pi" Catalyst-Modified W:$BiVO_4$. *J. Am. Chem. Soc.* **2011**, *133*, 18370–18377.

(33) Seabold, J. A.; Choi, K.-S. Efficient and Stable Photo-Oxidation of Water by a Bismuth Vanadate Photoanode Coupled with an Iron Oxyhydroxide Oxygen Evolution Catalyst. *J. Am. Chem. Soc.* **2012**, *134*, 2186–2192.

(34) Kim, T. W.; Choi, K.-S. Nanoporous $BiVO_4$ Photoanodes with Dual-Layer Oxygen Evolution Catalysts for Solar Water Splitting. *Science* **2014**, *343*, 990–994.

(35) Chen, L.; Toma, F. M.; Cooper, J. K.; Lyon, A.; Lin, Y.; Sharp, I. D.; Ager, J. W. Mo-Doped $BiVO_4$ Photoanodes Synthesized by Reactive Sputtering. *ChemSusChem* **2015**, *8*, 1066–1071.

(36) Lichterman, M. F.; Shaner, M. R.; Handler, S. G.; Brunschwig, B. S.; Gray, H. B.; Lewis, N. S.; Spurgeon, J. M. Enhanced Stability and Activity for Water Oxidation in Alkaline Media with Bismuth Vanadate Photoelectrodes Modified with a Cobalt Oxide Catalytic Layer Produced by Atomic Layer Deposition. *J. Phys. Chem. Lett.* **2013**, *4*, 4188–4191.

(37) Zhong, M.; Hisatomi, T.; Kuang, Y.; Zhao, J.; Liu, M.; Iwase, A.; Jia, Q.; Nishiyama, H.; Minegishi, T.; Nakabayashi, M.; et al. Surface Modification of $CoO_x$ Loaded $BiVO_4$ Photoanodes with Ultrathin P -Type NiO Layers for Improved Solar Water Oxidation. *J. Am. Chem. Soc.* **2015**, *137*, 5053–5060.

(38) Chang, X.; Wang, T.; Zhang, P.; Zhang, J.; Li, A.; Gong, J. Enhanced Surface Reaction Kinetics and Charge Separation of P–n Heterojunction $Co_3O_4/BiVO_4$ Photoanodes. *J. Am. Chem. Soc.* **2015**, *137*, 8356–8359.

(39) Jia, Q.; Iwashina, K.; Kudo, A. Facile Fabrication of an Efficient $BiVO_4$ Thin Film Electrode for Water Splitting under Visible Light Irradiation. *Proc. Natl. Acad. Sci.* **2012**, *109*, 11564–11569.

(40) Kim, T. W.; Choi, K.-S. Improving Stability and Photoelectrochemical Performance of $BiVO_4$ Photoanodes in Basic Media by Adding a $ZnFe_2O_4$ Layer. *J. Phys. Chem. Lett.* **2016**, *7*, 447–451.

(41) Wurfel, U.; Cuevas, A.; Wurfel, P. Charge Carrier Separation in Solar Cells. *IEEE J. Photovoltaics* **2015**, *5*, 461–469.

(42) Barroso, M.; Mesa, C. a; Pendlebury, S. R.; Cowan, A. J.; Hisatomi, T.; Sivula, K.; Gratzel, M.; Klug, D. R.; Durrant, J. R. Dynamics of Photogenerated Holes in Surface Modified α-$Fe_2O_3$ Photoanodes for Solar Water Splitting. *Proc. Natl. Acad. Sci.* **2012**, *109*, 15640–15645.

(43) Yang, J.; Walczak, K.; Anzenberg, E.; Toma, F. M.; Yuan, G.; Beeman, J.; Schwartzberg, A.; Lin, Y.; Hettick, M.; Javey, A.; et al. Efficient and Sustained Photoelectrochemical Water Oxidation by Cobalt Oxide/Silicon Photoanodes with Nanotextured Interfaces. *J. Am. Chem. Soc.* **2014**, *136*, 6191–6194.

(44) McDonald, K. J.; Choi, K.-S. A New Electrochemical Synthesis Route for a BiOI Electrode and Its Conversion to a Highly Efficient Porous $BiVO_4$ Photoanode for Solar Water Oxidation. *Energy Environ. Sci.* **2012**, *5*, 8553.

(45) Liu, Y.; Zhao, L.; Li, M.; Guo, L. $TiO_2$/CdSe Core-Shell Nanofiber Film for Photoelectrochemical Hydrogen Generation. *Nanoscale* **2014**, *6*, 7397.

(46) Johnson, R. W.; Hultqvist, A.; Bent, S. F. A Brief Review of Atomic Layer Deposition: From Fundamentals to Applications. *Mater. Today* **2014**, *17*, 236–246.

(47) George, S. M. Atomic Layer Deposition: An Overview. *Chem. Rev.* **2010**, *110*, 111–131.

(48) Hu, S.; Shaner, M. R.; Beardslee, J. A.; Lichterman, M.; Brunschwig, B. S.; Lewis, N. S. Amorphous $TiO_2$ Coatings Stabilize Si, GaAs, and GaP Photoanodes for Efficient Water Oxidation. *Science* **2014**, *344*, 1005–1009.

(49) Lee, M. H.; Takei, K.; Zhang, J.; Kapadia, R.; Zheng, M.; Chen, Y.-Z.; Nah, J.; Matthews, T. S.; Chueh, Y.-L.; Ager, J. W.; et al. P-Type InP Nanopillar Photocathodes for Efficient Solar-Driven Hydrogen Production. *Angew. Chemie Int. Ed.* **2012**, *51*, 10760–10764.

(50) Dendooven, J.; Pulinthanathu Sree, S.; De Keyser, K.; Deduytsche, D.; Martens, J. A.; Ludwig, K. F.; Detavernier, C. In Situ X-Ray Fluorescence Measurements During Atomic Layer Deposition: Nucleation and Growth of $TiO_2$ on Planar Substrates and in Nanoporous Films. *J. Phys. Chem. C* **2011**, *115*, 6605–6610.

(51) Gilbert, J. B.; Rubner, M. F.; Cohen, R. E. Depth-Profiling X-Ray Photoelectron Spectroscopy (XPS) Analysis of Interlayer Diffusion in Polyelectrolyte Multilayers. *Proc. Natl. Acad. Sci.* **2013**, *110*, 6651–6656.

(52) Luo, W.; Yang, Z.; Li, Z.; Zhang, J.; Liu, J.; Zhao, Z.; Wang, Z.; Yan, S.; Yu, T.; Zou, Z. Solar Hydrogen Generation from Seawater with a Modified $BiVO_4$ Photoanode. *Energy Environ. Sci.* **2011**, *4*, 4046.

(53) Xiao, S.; Chen, H.; Yang, Z.; Long, X.; Wang, Z.; Zhu, Z.; Qu, Y.; Yang, S. Origin of the Different Photoelectrochemical Performance of Mesoporous $BiVO_4$ Photoanodes between the $BiVO_4$ and the FTO Side Illumination. *J. Phys. Chem. C* **2015**, *119*, 23350–23357.

(54) Cooper, J. K.; Gul, S.; Toma, F. M.; Chen, L.; Glans, P.-A.; Guo, J.; Ager, J. W.; Yano, J.; Sharp, I. D. Electronic Structure of Monoclinic $BiVO_4$. *Chem. Mater.* **2014**, *26*, 5365–5373.

(55) Zhang, N.; Shi, J.; Mao, S. S.; Guo, L. $Co_3O_4$ Quantum Dots: Reverse Micelle Synthesis and Visible-Light-Driven Photocatalytic Overall Water Splitting. *Chem. Commun.* **2014**, *50*, 2002.

(56) Newville, M. *Fundamentals of XAFS*; Mineral Soc America, 2014; Vol. 78.

(57) Kanan, M. W.; Yano, J.; Surendranath, Y.; Dincă, M.; Yachandra, V. K.; Nocera, D. G. Structure and Valency of a Cobalt-Phosphate Water Oxidation Catalyst Determined by in Situ X-Ray Spectroscopy. *J. Am. Chem. Soc.* **2010**, *132*, 13692–13701.

(58) Ha, D.-H.; Moreau, L. M.; Honrao, S.; Hennig, R. G.; Robinson, R. D. The Oxidation of Cobalt Nanoparticles into Kirkendall-Hollowed CoO and $Co_3O_4$: The Diffusion Mechanisms and Atomic Structural Transformations. *J. Phys. Chem. C* **2013**, *117*, 14303–14312.

(59) Bergmann, A.; Martinez-Moreno, E.; Teschner, D.; Chernev, P.; Gliech, M.; de Araújo, J. F.; Reier, T.; Dau, H.; Strasser, P. Reversible Amorphization and the Catalytically Active State of Crystalline $Co_3O_4$ during Oxygen Evolution. *Nat. Commun.* **2015**, *6*, 8625.

(60) Wang, H.-Y.; Hung, S.-F.; Chen, H.-Y.; Chan, T.-S.; Chen, H. M.; Liu, B. In Operando Identification of Geometrical-Site-Dependent Water Oxidation Activity of Spinel $Co_3O_4$. *J. Am. Chem. Soc.* **2016**, *138*, 36–39.

(61) Chen, J.; Wu, X.; Selloni, A. Electronic Structure and Bonding Properties of Cobalt Oxide in the Spinel Structure. *Phys. Rev. B* **2011**, *83*, 245204.

(62) Pattengale, B.; Ludwig, J.; Huang, J. Atomic Insight into the W-Doping Effect on Carrier Dynamics and Photoelectrochemical Properties of $BiVO_4$ Photoanodes. *J. Phys. Chem. C* **2016**, *120*, 1421–1427.

(63) Greiner, M. T.; Helander, M. G.; Tang, W.-M.; Wang, Z.-B.; Qiu, J.; Lu, Z.-H. Universal Energy-Level Alignment of Molecules on Metal Oxides. *Nat. Mater.* **2011**, *11*, 76–81.

(64) Zhang, Z.; Yates, J. T. Band Bending in Semiconductors: Chemical and Physical Consequences at Surfaces and Interfaces. *Chem. Rev.* **2012**, *112*, 5520–5551.

## TABLE OF CONTENTS (TOC) IMAGE